Tumor radiation response enhancement by acoustical stimulation of the vasculature

Gregory J. Czarnota[a,b,c,d,1], Raffi Karshafian[c,d,e], Peter N. Burns[c,d], Shun Wong[a,b,d], Azza Al Mahrouki[a,c], Justin W. Lee[a,b,c,d], Amanda Caissie[a,c], William Tran[a], Christina Kim[a,c,d], Melissa Furukawa[a,c], Emily Wong[a,c], and Anoja Giles[a,c]

[a]Radiation Oncology, Sunnybrook Health Sciences Centre, Toronto, ON, Canada M4N 3M5; [b]Department of Radiation Oncology, University of Toronto, Toronto, ON, Canada M4N 3M5; [c]Imaging Research, Sunnybrook Health Sciences Centre, Toronto, ON, Canada M4N 3M5; [d]Department of Medical Biophysics, University of Toronto, Toronto, ON, Canada M4N 3M5; and [e]Department of Physics, Ryerson University, Torotno, ON, Canada M5B 2K3

Edited by Floyd Dunn, University of Illinois, Tucson, AZ, and approved June 6, 2012 (received for review January 24, 2012)

We have discovered that ultrasound-mediated microbubble vascular disruption can enhance tumor responses to radiation in vivo. We demonstrate this effect using a human PC3 prostate cancer xenograft model. Results indicate a synergistic effect in vivo with combined single treatments of ultrasound-stimulated microbubble vascular perturbation and radiation inducing an over 10-fold greater cell kill with combined treatments. We further demonstrate with experiments in vivo that induction of ceramide-related endothelial cell apoptosis, leading to vascular disruption, is a causative mechanism. In vivo experiments with ultrasound and bubbles permit radiation doses to be decreased significantly for comparable effect. We envisage this unique combined ultrasound-based vascular perturbation and radiation treatment method being used to enhance the effects of radiation in a tumor, leading to greater tumor eradication.

bioeffects | contrast agent | vascular disruption | radiosensitization

Radiation is a major anticancer therapy and is currently used to treat a majority of patients with different tumors (1). Radiobiology recognizes that radiation acts primarily by damaging cancer cell DNA leading to cell death (2). However, recent data indicate that radiation-induced endothelial cell apoptosis (3) can lead to vascular destruction and secondary tumor cell death (4). It has been demonstrated that this vascular death is ceramide-mediated and may be an important mechanism of tumor kill in vivo (5). In this alternative mechanism tumor cells die secondary to damage caused by radiation to the microvasculature. These results have been reproduced in lung and brain tissue (6). In contrast, basic fibroblast growth factor (bFGF), a vascular protective agent, enhances epithelial stem cell survival from effects of whole-body irradiation (7). Paris et al. (3) also suggest that early-phase microvascular endothelial apoptosis is mandatory for tumor cure. In this model it is suggested that radiation-induced lesions in tumor cells are not lethal by themselves, but their conversion to lethal damage is tightly connected to endothelial cell function and the *asmase* (acid sphingomyelinase) gene. Other studies (8, 9) suggest that endothelial cell death occurs with single doses (>8–10 Gy) of ionizing radiation via an *asmase*-dependent pathway whereas with fractionated radiation (1.8–3 Gy/fraction) effects may be modulated differently.

Hyperthermia has been used to enhance successfully the effects of radiation (2) and is currently being pursued for liposomal-mediated drug delivery (10), simultaneous thermal treatment with radiation (11), and MRI guidance for higher-powered thermal ablation (12). It has demonstrated excellent clinical results (13). Other newer vascular-targeted methods include drug-based treatments with vascular disrupting agents (reviewed in ref. (14)).

Rather than using a traditional pharmacological or hyperthermia approach to perturb the vascular endothelial lining, we took the approach of perturbing the endothelial lining of the vasculature with ultrasound- and microbubble-mediated mechanical disruption. Microbubbles comprise micron-sized spheres of gas, usually a perfluorocarbon, within a thin shell of stabilizing material (such as a protein or lipid). The median bubble diameter is about 3 μm, which is small enough for the bubbles to pass through the systemic circulation following peripheral venous injection. When activated by specific ultrasound frequencies, microbubbles can exhibit resonance behavior and, under different conditions, nonlinear responses. In addition, they can be burst with low-mechanical index pulses of ultrasound. Microbubble contrast agents are given intravenously and are typically used to facilitate the delineation of micron range blood vessels in tumor models (15–18). Such agents are finding new uses as a consequence of the perturbations they cause in the structural integrity of cells and tissue. These include permeabilizing the blood–brain barrier for drug delivery, permeabilizing cells to introduce therapeutic agents or genes, and breaking down intravascular thrombi (19–21).

We demonstrate here that low mechanical index ultrasound-mediated excitation of microbubbles can enhance the effects of radiation in vitro and supraadditively in vivo using histological and functional assays of cell death and tumor growth delay experiments. Data obtained from experiments in vitro indicate that, under these ultrasound-exposure conditions, ceramide formation is induced by microbubble interactions with cells and associated with endothelial cell apoptosis. This is a known mechanism for radiation-based, ceramide-related endothelial cell death (22). Endothelial cell death in vivo caused by microbubble perturbation of tumor microvasculature leads to a pronounced vascular disruption and a 10-fold enhancement of tumor cell death when combined with single radiation treatments. Experiments indicate that single 2-Gy doses of radiation can lead to more than 40% tumor volume kill. Treatments with multiple fractions of the combined modalities demonstrate that ineffective doses of radiation can be made more effective in terms of tumor growth delay and mouse survival.

We propose that such combined treatments lead to vascular cell death, which then secondarily induces tumor cell kill, and that such treatments can be used to increase the efficacy of cancer treatments.

Results

Single-Fraction Experiments. We tested the hypothesis that combined mechanical disruption of endothelial cells and radiation can result in synergistic tumor cell kill in vivo. For ultrasound treatments, PC3 prostate cancer xenograft-bearing mice were given microbubbles intravenously, which were stimulated using

Author contributions: G.J.C., R.K., and C.K. designed research; G.J.C., R.K., S.W., A.A.M., J.W.L., A.C., W.T., C.K., M.F., E.W., and A.G. performed research; G.J.C. and P.N.B. contributed new reagents/analytic tools; G.J.C., S.W., A.A.M., J.W.L., A.C., W.T., C.K., M.F., E.W., and A.G. analyzed data; and G.J.C. and A.A.M. wrote the paper.

The authors declare no conflict of interest.

This article is a PNAS Direct Submission.

[1]To whom correspondence should be addressed. E-mail: Gregory.Czarnota@sunnybrook.ca.

See Author Summary on page 11904 (volume 109, number 30).

This article contains supporting information online at www.pnas.org/lookup/suppl/doi:10.1073/pnas.1200053109/-/DCSupplemental.

ultrasound to cause endothelial cell perturbations only within tumor vasculature. Three sets of mice ($n = 36 \times 3$), in addition to controls, were used noninvasively to investigate acute effects, longitudinal effects, and blood flow.

Experimental conditions included no, low, and high concentrations of microbubbles activated by ultrasound. Each of these was coupled with 0, 2, or 8 Gy of radiation given in one fraction, resulting in nine experimental conditions with four mice per group ($n = 36$). Mice were treated intentionally with combined single fractions to investigate combined effects. Other control conditions, including ultrasound exposure in the absence of bubbles and bubble injections without ultrasound, were investigated ($n = 4$ each).

In order to ensure that microbubbles replenished the microvasculature between pulses designed to cause microbubble disruption, the ultrasound pulse sequence for mouse treatments was transmitted using a 10% duty cycle within a 50-ms window every 2 s for a total active insonification time of 750 ms over 5 min for an overall duty cycle of 0.25%. Microbubble disruption was carried out at a diagnostic ultrasound exposure range using a pressure of 570 kPa for a mechanical index of 0.76. These parameters were chosen to prevent tissue heating and thermal damage, which are theoretically negligible at these conditions.

The first set of mice was killed for histological analysis 24 h after treatment. This time was selected to maximize potential tumor cell death secondary to gross vascular disruption caused by endothelial cell apoptosis.

Results indicated that the combination of ultrasound-stimulated microbubble treatment with radiation resulted in a significant induction of cell death. Representative data presented in Fig. 1 indicate extensive increases in cell death with combined treatments. Treatment with 0 Gy, or a single 2-or 8-Gy fraction of radiation alone resulted in minimal apoptotic or necrotic cell death ($4 \pm 2\%$ death for 2 Gy, mean $\pm$ SE) as did ultrasound-activated microbubble treatment alone ($10 \pm 4\%$ death for the low bubble concentration). In contrast, the combination of these resulted in obvious macroscopic regions of apoptotic and necrotic cell death in the area of ultrasound microbubble activation occupying approximately $40 \pm 8\%$ or more of the tumor cross-sectional area (Fig. 1) for the 2-Gy dose combined with the low microbubble treatment with ultrasound. The combined 2-Gy and high microbubble concentration resulted in more cell death ($44 \pm 13\%$), and the combination of 8-Gy and the high microbubble concentration resulted in even more cell death ($70 \pm 8\%$). Quantification of tumor cell death indicated a supraadditive effect between radiation and the ultrasound treatments (Fig. 1*C*) with increasing apoptosis observed with the combined treatments. Quantitative analysis of histopathology results confirmed a supraadditive effect between the ultrasound-activated microbubble treatments and the effect of radiation. There were nonlinear increases in macroscopic measurements of cell death evident when the ultrasound-activated microbubble treatments were combined with radiation treatments. The combination of the two treatments also led to nonlinear increases in the number of apoptotic cells (Fig. 1*D*). Additional control treatments with ultrasound alone, and with injected microbubbles in the absence of ultrasound, demonstrated no significant difference in comparison to untreated mice ($P < 0.05$). Statistical analysis by two-way ANOVA indicated a significant effect of radiation ($P = 0.0002$) and effect of microbubble treatments ($P < 0.0001$), and indicated an interaction between radiation and microbubble treatment ($P < 0.0002$). The combined 2-Gy and microbubble treatments were significantly different compared to 2-Gy alone or ultrasound-activated microbubble treatments alone, for the ultrasound-activated low and high microbubble concentration treatments, respectively (all P values <0.0001). This was also observed for the combined 8-Gy and microbubbles treatments compared to 8-Gy or ultrasound microbubble treatments alone (all P values <0.0001).

In order to investigate the mechanism behind this enhancement of cell death we utilized noninvasive imaging techniques to track effects on the vasculature as well as immunohistochemical histology methods. Power Doppler micro-ultrasound imaging was carried out in a separate cohort of mice under the same experimental conditions ($n = 36$). Selected representative results are presented in Fig. 2. Doppler data demonstrated moderate vascular disruption with ultrasound and microbubbles, and with 8-Gy radiation doses ($20 \pm 21\%$ and $20 \pm 32\%$ decrease in Doppler vascular index, respectively). Significant reductions in blood flow at 24 h for the combined ultrasound-activated microbubble and radiation treatments were observed, suggestive of vascular disruption ($65 \pm 8\%$ decrease in Doppler vascular index). The combination with ultrasound-stimulated microbubbles and radiation was significantly better in flow diminishment compared to the single treatments ($P < 0.001$) (Fig. 2*A*). The effect of the combination treatments was more consistent with a smaller standard error compared to individual treatments. Corresponding immunohistochemistry under high-power microscopy indicated that ultrasound-activated microbubble treatments resulted in microscopic localized appearances consistent with endothelial cell apoptosis, whereas combined ultrasound-activated microbubble and radiation treatments resulted in near-total cell death of endothelial cells and tumor cells that was not apparent at the other experimental conditions (Fig. 2*A*).

Analysis (ANOVA) indicated that in situ end-labeling (ISEL) staining levels for ultrasound-stimulated microbubble treatment in combination with radiation ($70 \pm 8\%$) were significantly different in comparison to radiation alone ($4 \pm 2\%$) or ultrasound-stimulated microbubble exposure alone ($36 \pm 12\%$) (both $P < 0.001$) 24 h after treatment for the higher microbubble concentration.

Immunohistochemical staining of von Willebrand factor revealed enhanced leakage from the vasculature with the combined ultrasound-activated microbubble and radiation treatments, further suggestive of vascular disruption (Fig. 2*A*). In order to investigate the mode of endothelial cell death being induced by the ultrasound treatments in the presence of microbubbles, confocal microscopy of triple immunohistochemical—stained sections of ultrasound-activated microbubble—treated xenograft tumors sections confirmed the induction of apoptosis in endothelial cells in tumors treated with ultrasound and microbubbles (Fig. 2*B*). Analysis (ANOVA) indicated that staining levels for ultrasound-stimulated microbubble treatment (low bubble concentration) in combination with radiation ($8 \pm 1\%$) were significantly different in comparison to radiation alone ($2 \pm 1\%$) or ultrasound-stimulated microbubble exposure alone ($6 \pm 1\%$) (both $P < 0.001$) 24 h after treatment. These values were for the low microbubble concentration and were consistent in general with ISEL staining of whole tumor at that concentration of microbubbles: $18 \pm 15\%$ apoptosis for radiation and ultrasound and microbubbles, $1 \pm 4\%$ for radiation alone, and $7 \pm 4\%$ apoptotic index for ultrasound-stimulated microbubble exposure alone (Fig. 1*C*).

Targeted-Microbubble and bFGF Experiments. In order to investigate the effect of microbubble proximity to endothelial cells in the observed radiation-enhancing effect experiments with nontargeted and VEGFR2-targeted (vascular endothelial growth factor receptor) microbubbles indicated increases in cell death with the targeted microbubbles ($P = 0.005$). For nontargeted treatments, pretreatment of animals with bFGF diminished the cell death that microbubble treatments induced. In addition, there was no difference between bFGF-treated animals when treated by ultrasound-stimulated microbubbles and untreated control, in terms of cell death ($P = 0.24$) (Fig. S1).

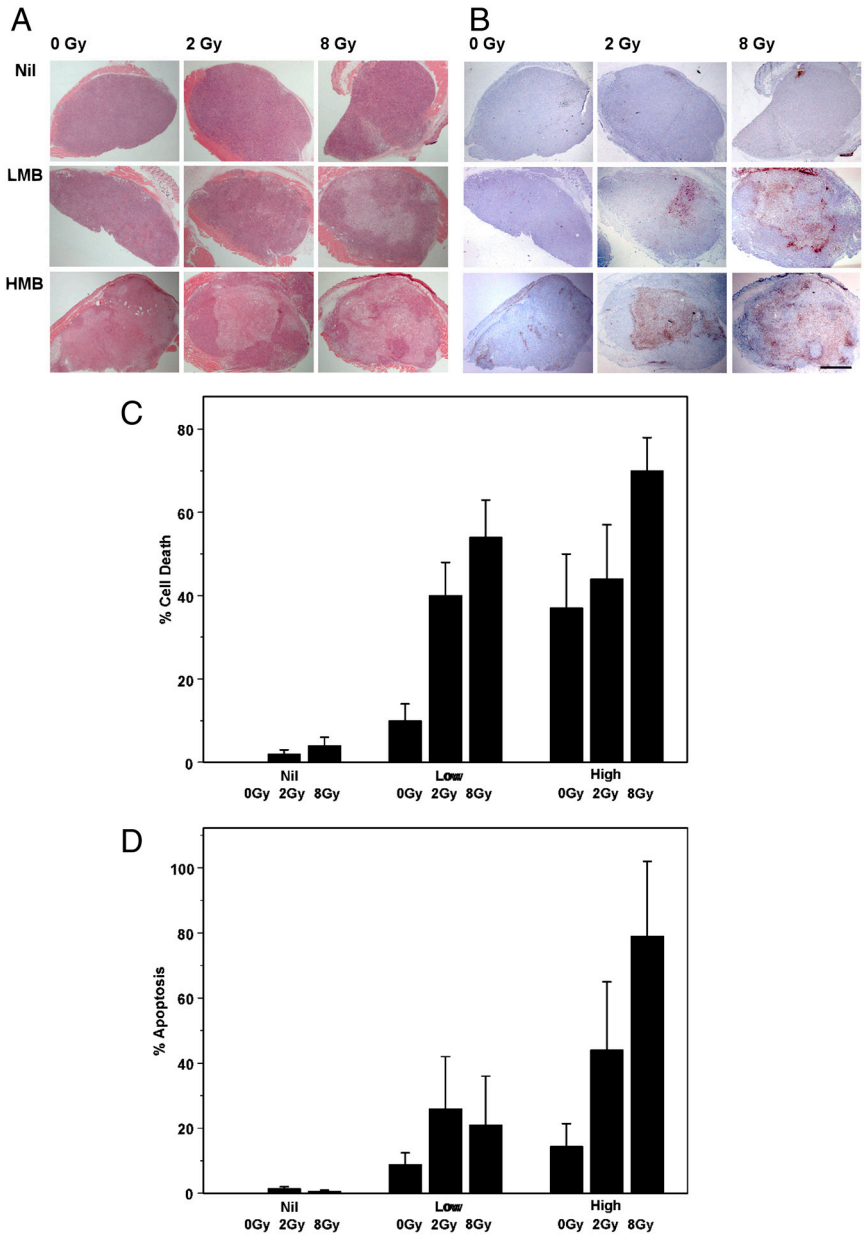

Fig. 1. Cell death assessments. Representative hematoxylin and eosin (*A*) and corresponding ISEL-stained (*B*) sections of PC3 prostate tumors treated with radiation and/or ultrasound-activated microbubbles. Columns represent 0, 2, and 8 Gy of radiation exposure from left to right. Rows indicate no (Nil), low concentration microbubble exposure (LMB), and high microbubble exposure (HMB) from top to bottom, respectively. Exposure to radiation alone (*Top*) shows no appreciable cell death in the stained sections or the ISEL-stained areas (orange staining). Microbubble-alone exposure demonstrated minor cell death at the low concentration but, at the higher concentration, appeared to have a diffuse effect. The addition of radiation to the microbubble treatments led to significant detectable cell death, appearing as clear zones in the hematoxylin- and eosin-stained slides. (*C*) Data obtained from low-power microscope views of whole tumor sections quantifying the extent of ISEL staining for each treatment. These data demonstrate an enhancement of tumor cell death when radiation ($4 \pm 2\%$ ISEL + staining, 2 Gy) is combined with ultrasound-activated microbubble treatment ($10 \pm 4\%$ ISEL + staining, low microbubble concentration) resulting in $40 \pm 10\%$ cell death when combined. (*D*) Data on apoptotic cells detected from stained sections based on morphological observation at high power. Scale bar, 2 mm.

Exposure Experiments. In order to investigate the effect of ultrasound-stimulated microbubble exposure, experiments were conducted in which the concentration of microbubbles was varied (Fig. 3). For experiments, the microbubble concentration was varied from nil, to 0.01, and 0.1 of the low concentration, the low concentration, and to the high concentration. These concentrations were combined with 0, 2, and 8 Gy. Statistical analysis using ANOVA indicated an interaction accounting for 11% of the total observed effect ($P < 0.001$). Analysis with ANOVA indicated that radiation dose accounted for 10% of the effect ($P < 0.001$) and microbubble dose accounted for 70% of the observed effect ($P < 0.001$) ($n = 4$ for all groups). Treatment effects were present at 0.01 of the low concentration (approximate clinical imaging concentration) of microbubbles but increased at the higher concentrations. With the 2-Gy doses, exposure to the low and high microbubble concentrations produced equivalent results with better results at the higher concentration of bubbles combined with 8-Gy radiation treatment.

Timing Experiments. Effects of ultrasound-stimulated microbubble exposure and resultant effects on cell death and micro-Doppler-detected blood flow were investigated. This modality was investigated alone and with a sequence of a time delay introduced with subsequent radiation treatment (0, 3, 6, 12, and 24 h) ($n = 4$ for all groups). Treatment with ultrasound-stimulated microbubbles indicated maximal cell death, detected using ISEL staining when the two treatments were separated by 6 h, which coincided with a maximal decrease in detected micro-Doppler blood-flow signal. Radiation at that time resulted in a maximal effect 24 h later, in terms of ISEL-detected cell death and disruption of blood flow-linked micro-Doppler-detected signal (Fig. 4*A* and *B*). The data imply a 9-h window for radiation therapy after microbubble exposure with no statistically significant difference between results from 3 to 12 h.

For time interval experiments ANOVA indicated a statistically significant radiation effect ($P < 0.0001$), a statistically significant microbubble effect ($P < 0.0001$), and an interaction between the two treatments ($P < 0.0001$) for cell death and blood flow disruption each.

Single-Fraction Growth Delay. Another cohort of mice ($n = 36$) was treated with the same nine conditions used initially for single

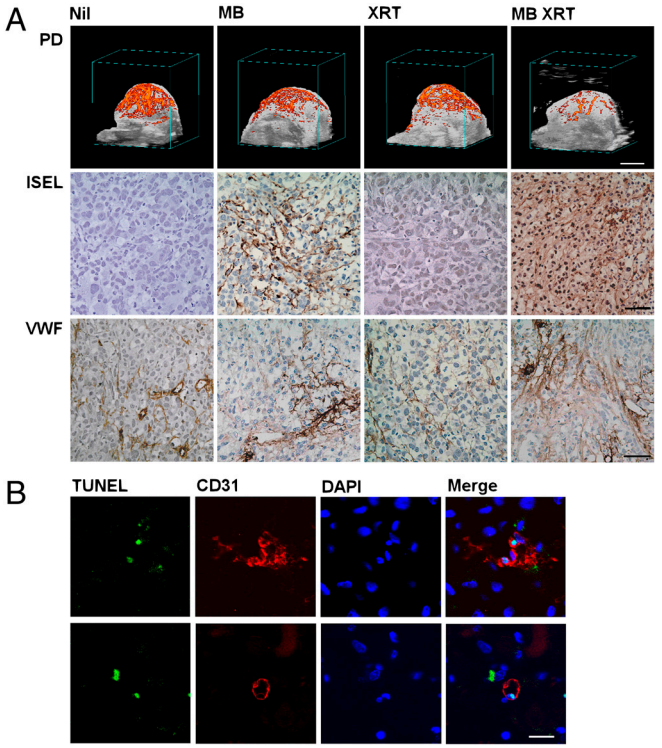

Fig. 2. Power Doppler ultrasound imaging and high-magnification immunohistochemical data for radiation and ultrasound treatments. (*A*) Rows show power Doppler images (PD), ISEL high-magnifications data (ISEL), and von Willebrand factor staining (VWF) for vasculature. Columns indicate data for no treatment (Nil), ultrasound-activated microbubbles (MB), 8-Gy radiation (XRT), and microbubble and radiation treatments combined (MB XRT). Power Doppler data obtained at 20 MHz indicate blood flow disruption with treatments ($20 \pm 37\%$ decrease with microbubble ultrasound treatment, $18 \pm 22\%$ decrease with radiation alone, and $65 \pm 8\%$ decrease with the combined treatments; mean $\pm$ standard error). The difference between the single treatments and the combined ultrasound-stimulated microbubble treatment was significant ($P < 0.05$). Scale bar, 2 mm. Staining with ISEL demonstrates a stranding suggestive of vascular distributions with microbubble treatments. Combined treatments result in what appears to be complete ISEL + cellular staining. Scale bar, 60 microns. Staining with von Willebrand factor suggests vascular disruption with bland smearing from leaking serum in the combined treatment specimen. Scale bar, 60 microns. (*B*) Triple staining for endothelial cell apoptosis with TUNEL + apoptotic nuclei, CD31 vascular delineation, and DAPI for nuclear positions for tumor samples treated with the higher concentration of microbubbles. Images (Merge) indicate the presence of apoptotic nuclei (cyan) associated with vascular endothelial cells (red). Scale bar, 20 microns.

treatments, except that mice were followed longitudinally after treatments for growth delay effects of single treatments, bearing in mind that ultrasound and microbubble treatments as delivered resulted in a viable tumor rim. At 5 d, combined ultrasound-activated microbubble and 2-Gy or 8-Gy radiation treatments yielded the greatest growth delay (Fig. S2). Ultrasound-activated microbubble treatments yielded a similar delay in xenograft tumor growth. Radiation treatments alone were less effective at arresting tumor growth, with tumor growth still evident at 5 d duration. At 20 d after treatment with ultrasound-activated microbubble treatments alone or combined with 2 Gy there was rebound growth of tumor xenografts. The combined ultrasound-activated microbubble treatment and 8-Gy radiation treatment effectively inhibited tumor growth whereas 8 Gy alone began to show regrowth at 21 d.

Growth 5 d after combined treatment with 2-Gy radiation and ultrasound-stimulated microbubbles was significantly different from 2 Gy alone ($P < 0.01$) but not 8 Gy. Ultrasound-stimulated microbubble treatment alone was different compared to 2 Gy or

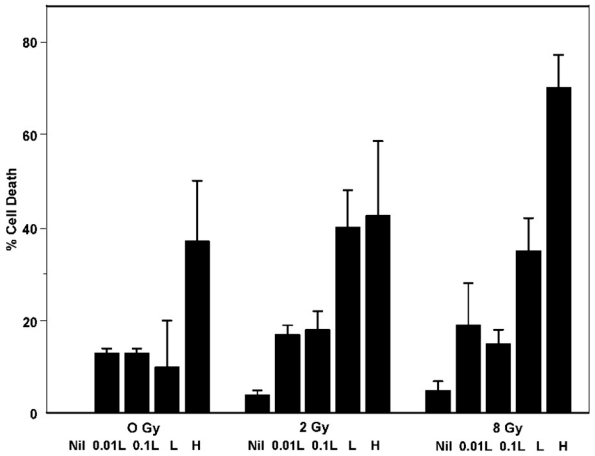

Fig. 3. (*A*) Quantitative analysis of cell death in response to microbubble exposure with different radiation doses. Percentage ISEL + staining from four tumors per group is shown with different microbubble concentrations administered to mice. For microbubble concentrations: Nil indicated no treatment; 0.01 L and 0.1 L indicate dilutions of the low microbubble concentration (L); and (H) indicates the high microbubble concentration used. Different radiation doses include 0, 2, and 8 Gy, as labeled.

8 Gy alone ($P < 0.01$). At 20 d after growth rebound there was no difference in growth delay between 2 Gy combined with ultrasound-stimulated microbubbles compared to 2 Gy alone. Ultrasound-stimulated microbubble treatment alone was not different compared to 2 Gy and had less growth delay than 8 Gy alone ($P < 0.01$). There was no difference in growth delay between ultrasound-stimulated treatment with 2 Gy in comparison to 8 Gy ($P < 0.05$).

Multiple-Fraction Growth Delay. Analysis of associated growth and survival curves and Ki-67 activity (as a marker of cellular proliferation) is presented in Fig. 5 and Fig. S3. Analysis of survival curves to mouse death or modified human endpoint or 2-cm tumor size indicated that they were significantly different ($P < 0.05$) with mean survivals of 10 ± 1, 19 ± 1, 20 ± 3, 25 ± 3, and 28 ± 0 d (mean $\pm$ standard error) for mice receiving no treatment, and treatment with the 2-Gy fractionation scheme [biological effective dose ($\alpha/\beta = 10$), BED(10) = 28.8 Gy], the ultrasound-stimulated microbubble regimen, the 3-Gy fractionation scheme [BED(10) = 58.5 Gy], and the combined ultrasound-stimulated microbubble and 2-Gy radiation fractionation regimen. Growth delay data indicated there was no significant difference between 2 Gy combined with ultrasound-stimulated microbubbles compared to the 3-Gy regimen.

For analyses of growth delay at day 21, the 2-Gy regimen combined with ultrasound-stimulated microbubbles was significantly different from 2 Gy alone ($P = 0.03$) and significantly different from the ultrasound treatments alone ($P = 0.02$). There was no significant difference in terms of growth delay at day 21 between the 2-Gy regimen combined with ultrasound-stimulated microbubbles and the 3-Gy regimen. Adding ultrasound-stimulated microbubbles to the 3-Gy regimen made no statistically significant difference in terms of growth delay. Analysis results using the nonparametric Mann–Whittney analysis were equivalent.

Further analysis using Ki-67 labeling (Fig. 4) indicated that the ultrasound-stimulated microbubble treatment in combination with ultrasound was significantly different in comparison to the 2-Gy regimen alone ($P < 0.001$). There was no statistically significant difference between this combined regimen and the 3-Gy radiation alone regimen ($P > 0.05$). Analysis using ANOVA indicated ($P < 0.007$) an interaction between radiation and microbubble treatment.

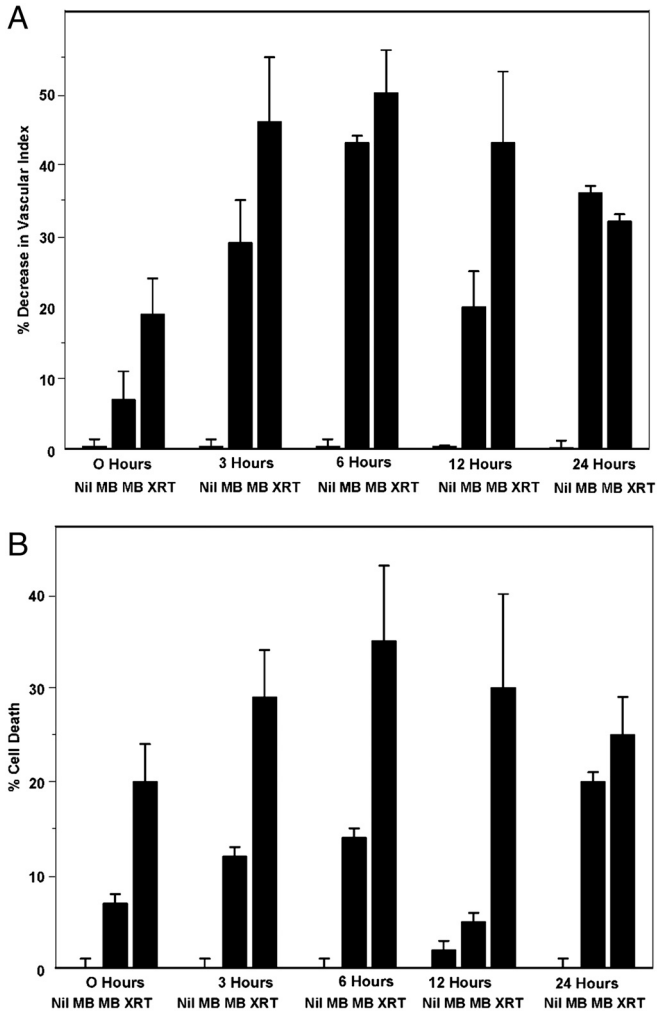

Fig. 4. (*A*) Quantitative analysis of cell death in response to timing between microbubble exposure and radiation treatment. Decrease in micro-power Doppler data measured vascular index with microbubbles and combined treatment. Nil, no treatment imaged before and 24 h later; MB, treatment with microbubbles only (low concentration) and killing of mice at the indicated times after microbubble exposure (0, 3, 6, 12, and 24 h); MBXRT, treatment with microbubbles and interval time as indicated between subsequent radiation treatment (8 Gy). (*C*) Resulting ISEL+ cell death corresponding to treatments as described in *A*. For treatments with microbubbles alone, note the maximal effect on blood flow at 6 h and cell death after 6 h. Combined treatments follow a similar trend.

Ceramide and Sphingosine-1-Phosphate (S1P) Experiments. Analyses of experiments from an additional cohort of 75 animals ($n = 5$ mice per group) indicated increases in ceramide formation in vivo with microbubble exposure combined with radiation exposure (Fig. 6 *A* and *B*). Statistical analysis using ANOVA indicated that bubble dose accounted for 32% of the total effect ($P = 0.0003$). Radiation dose accounted for 32% of the effect ($P = 0.0004$). Compared to no treatment the combination of either the low concentration or the high concentration of microbubbles with 8 Gy resulted in significant ceramide staining ($P < 0.05$ and $P < 0.001$, respectively). This was not as apparent for treatments using ultrasound-stimulated bubbles alone or radiation alone. Treatment with 8 Gy alone resulted in ceramide increases that were obvious but not significant. In the presence of S1P, which inhibits ceramide synthesis, increases were not apparent (Fig. 6 *C* and *D*). Statistical analysis indicated no significant increases in ceramide for the 2-Gy or 8-Gy dose in the presence of the high microbubble concentration.

Corresponding analyses of cell death are presented in Fig. 7. Data indicate apoptotic cell death was induced by ultrasound-stimulated microbubbles when combined with radiation (as in Fig. 1) but inhibited by S1P exposure. Treatment with S1P, given 30 min before and 5 min after treatments, resulted in a diminishment of detected apoptotic cell death with no statistically significant difference between 0-, 2-, and 8-Gy treatments in the presence of S1P (as control) and ultrasound-stimulated microbubble exposure combined with 0-, 2-, and 8-Gy treatments in the presence of S1P. In the absence of S1P, ultrasound-stimulated microbubble exposure and 0-, 2-, and 8-Gy treatments exhibited statistically significant levels of cell death as before. Apoptotic cell morphology and ISEL staining was diminished in the presence of S1P (Fig. 7 *C* and *D*).

Discussion

Combined ultrasound-activated microbubble and radiation treatments exhibited a supraadditive effect in vivo but not in vitro, suggesting a physiological mechanism for the observed enhancement of radiation response. Histological and immunohistochemical analyses indicated predominantly vascular effects of the combined treatments consistent with microvascular disruption. Endothelial cell apoptosis was induced by ultrasound and microbubble treatments and enhanced with combined radiation treatments, leading to a reduction in blood flow and the induction of tumor cell death. Doppler micro-ultrasound analyses revealed significant reduction of blood flow to tumor treated with the two modalities in combination. The maximal interval time for synergistic interaction appeared to be 6 h for single fractions of combined treatments. Experiments with VEGFR2-targeted microbubbles demonstrated a greater effect compared to untargeted microbubbles. This was not surprising because targeted microbubbles are more likely to be in close proximity to endothelial cells, which will increase oscillation-induced mechanical damage to cells. Protection of the vasculature with bFGF, a known radiation protector, also diminished microbubble effects. Effects were more prominent when treatment with ultrasound-stimulated microbubbles were combined with 8-Gy but also significantly present at 2-Gy radiation doses.

Treatments involving multiple fractions of radiation combined with ultrasound and microbubbles demonstrated a greater survival compared to radiation alone. Noncurative doses of radiation combined with ultrasound-stimulated microbubble treatment were at least as effective as curative doses of radiation. Results obtained in vivo with S1P as a ceramide cell death pathway inhibitor suggest ceramide is involved in responses to ultrasound microbubble treatments.

To our knowledge, this is a previously undescribed report of ultrasound-activated microbubbles being used to enhance radiation response. The combined treatments enhance the vascular response that radiation is recognized to induce, and enhance tumor cell death through a detectable perturbation of tumor microvasculature. Single treatments of ultrasound-activated microbubbles and radiation produced over 40% tumor cell death when ultrasound activation of bubbles was used in combination with 2 Gy of radiation in single treatments. Multiple fractions of 2-Gy radiation [24 Gy in 12 fractions given over 3 wk, BED(10) = 28.8 Gy] combined with ultrasound-stimulated microbubbles had a survival increase in comparison to that dose of radiation alone, and this was equivalent to a higher radiation ("curative") regimen of 45 Gy in 15 fractions [BED(10) = 58.5 Gy].

Potential cellular mechanisms include mechanical perturbation leading directly to endothelial cell apoptosis, cytokine stimulation, changes in ionic environment caused by vascular disruption, or activation of the ceramide pathway. Microbubbles and ultrasound may also cause biochemical reactions when depositing energy near cell membranes, leading to lipid reactions. However, the increases in ceramide production caused by microbubbles, particularly when combined with radiation, seemed to suggest activation of stress-

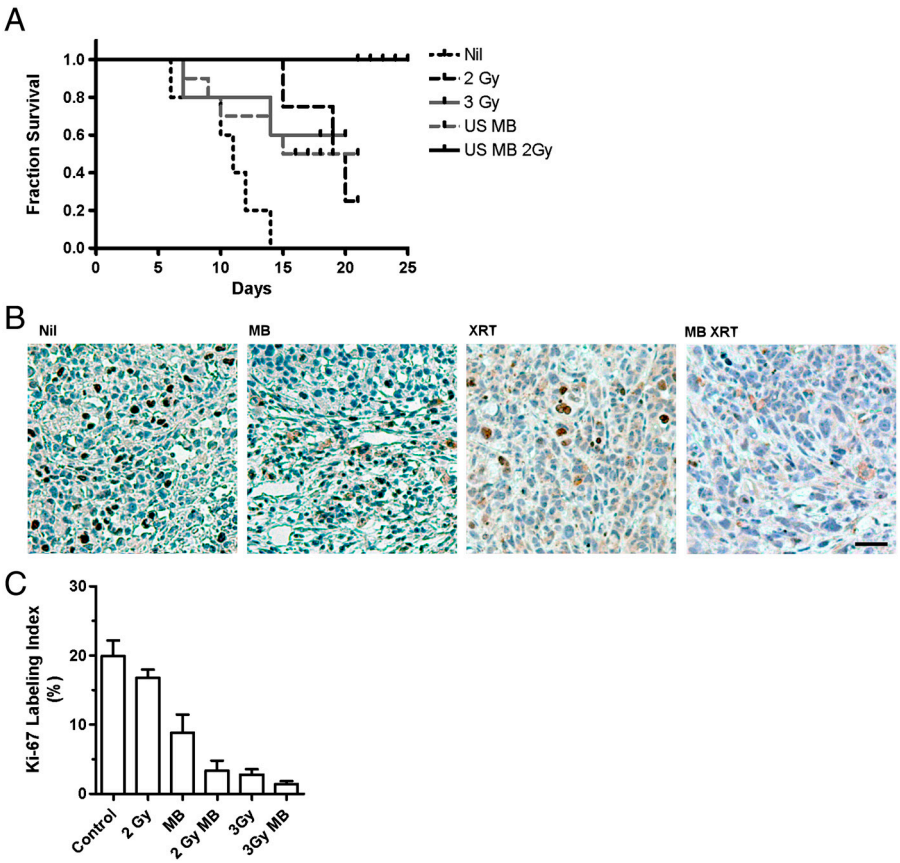

Fig. 5. Response assessments for multiple fraction experiments. (*A*) Survival data for multiple fraction treatments. Kaplan-Meier survival curves are presented for cohorts of mice treated with 2-Gy fractions (24 Gy in 12 fractions over 3 wk) [BED(10) = 28.8], 2-Gy fractions with two ultrasound-stimulated microbubble treatments weekly, 3-Gy fractions (45 Gy in 15 fractions over 3 wk) [BED(10) = 58.5], and ultrasound-stimulated microbubble treatments weekly (twice weekly for 3 wk). Endpoints were tumor at least doubling in size and reaching modified human-care endpoints (lack of ambulation, tumor greater than 2 cm in diameter). Results for the 3-Gy regimen with two ultrasound-stimulated microbubble treatments weekly are not presented, as the survival curve is very similar to that for the 3-Gy regimen. (*B*) High-magnification views of Ki-67 staining. Nil, no treatment; MB, ultrasound-activated microbubble treatment; XRT (2-Gy dose regimen); MB XRT, combined treatment. The 3-Gy dose regimen is not presented. Scale bar, 30 μm. (*C*) Ki-67 analysis by counting of representative tumor sections. The Ki-67-positive cell fraction for the combined treatment with the 2-Gy dose regimen combined with ultrasound microbubble treatments demonstrated a statistically significantly difference when compared to either the treatments with the 2-Gy dose regimen alone or the ultrasound microbubble treatments alone ($P < 0.05$). The difference between 3-Gy dose regimens with or without ultrasound treatment in comparison to the 2-Gy dose regimen combined with ultrasound microbubble treatment was not statistically significant ($P < 0.05$).

related lipid metabolism, likely in response to cell membrane damage. The ceramide pathway is well-recognized to be activated by various forms of energy as a stress response [reviewed in ref. (23)]. Inhibition of ceramide synthesis by S1P in vivo inhibited microbubble effects further, suggestive of a role of this signaling molecule in response to microbubble-induced vascular damage. Lipid biogenesis pathways involved in membrane repair may lead to the accumulation of ceramide and explain the observed endothelial cell apoptosis, which was inhibited in vivo by the use of a specific ceramide-induced apoptosis inhibitor. The ceramide generated in response to stressors, such as microbubble treatment, in addition to that produced through radiation, could contribute further to endothelial cell death vascular disruption in vivo. Within the tumor, cell death seemed to be secondary to vascular disruption with areas of central mixed apoptotic and necrotic death similar to vascular disrupting agents.

Microbubbles in the presence of ultrasound acted as a "biomechanical variant" of the well-characterized vascular disrupting agents (reviewed in ref. (13)). The remaining viable rim could be retreated with subsequent fractionated treatments, as was done, and may require different ultrasound parameters or higher-energy insonification to ensure effective treatments. In comparison to treatments with antiangiogenic agents (reviewed in ref. (24)), which often require long-term continual administration of drugs to which resistance can develop, the treatments here elicited large amounts of cell death within 24 h. Antiangiogenic treatments are believed to result in vascular normalization (25) through the "pruning" of cancer-related abnormal blood vessels. The treatments here, in contrast, rely on a mechanical disruption of vessels, which sensitizes endothelial cells to radiation. This leads to a vascular disruption (13) and secondary tumor cell death. A number of other therapeutic effects of ultrasound-stimulated microbubbles has been recently identified (reviewed in ref. (26)), and other ultrasound-induced bioeffects may be related similarly to cell membrane disruptions (27).

The experiments conducted here were mainly carried out using microbubble concentrations at 100–300 times greater than that used diagnostically, but also used concentrations at the diagnostic dose of microbubbles (Fig. 3). These lower concentrations exhibited a lesser effect when combined with radiation. However, these treatments were carried out with an overall duty cycle of 0.25% (750 ms insonifcation over 5 min). In order to compensate for lower microbubble concentrations, exposure to microbubble oscillations could be increased by increasing the duty cycle, because we posit the cell death-inducing effect is related to the number of bubbles insonified. The treatments with microbubbles in the presence of ultrasound caused a decrease in blood flow that seemed to recover in part near 12 h after treatment (Fig. 4). We suggest that this is caused by vascular repair. In treatments where radiation was combined, the data indicate greater levels of endothelial cell death and subsequent tumor cell death. Timing experiments indicated a similar 12-h period for interaction between microbubbles stimulated by ultrasound and radiation resulting in supraadditive effects present in regards to cell death.

Experiments were conducted here with xenografts in mice. Scale-up for larger tumors may require flow-related adjustments because tumor blood flow can be heterogeneous in humans. In addition, different tumor types can exhibit different levels of vascularity, which may also require microbubble exposure compensation.

In summary, combined ultrasound and radiation treatments were demonstrated to improve the effects of radiotherapy, which is commonly given in multiple-fraction treatments, such as those used in our study. This could be envisaged as a conformal method of enhancing radiation responses. Microbubble-activated ultrasound treatments could be focused in an image-guided manner to just the tumor alone, as is already done with high-power thermal treatments, minimizing normal tissue toxicity. Further, there could be a differential sensitivity in normal tissues as tumor microvasculature is functionally abnormal. Additionally, such

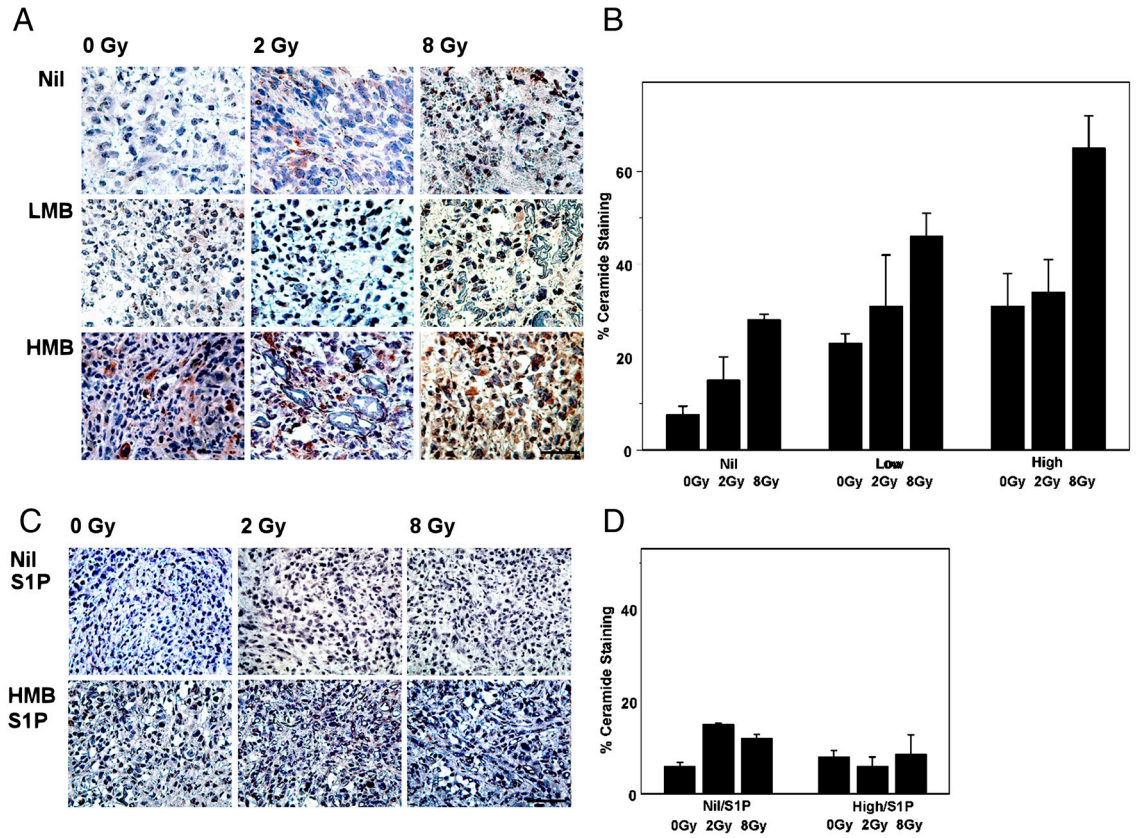

Fig. 6. In vivo ceramide staining data. (*A*) Representative ceramide staining of sections of PC3 prostate tumors treated with radiation and/or ultrasound-activated microbubbles. Columns represent 0, 2, and 8 Gy of radiation exposure from left to right. Rows indicate no (Nil), low-concentration microbubble exposure (LMB), and high microbubble exposure (HMB) from top to bottom, respectively. Exposure to radiation alone (*Top*) shows no appreciable ceramide formation except at the 8-Gy dose (brown staining). Microbubble-alone exposure demonstrated minor ceramide staining at the low concentration but, at the higher concentration, appeared to have a more prominent effect. The addition of radiation to the microbubble treatments led to detectable ceramide staining, greatest in the high microbubble concentration when combined with 8 Gy (diffuse brown staining). Scale bar, 200 microns. (*B*) Quantification of ceramide immunohistochemistry staining. Samples were assessed with respect to ceramide staining. Brown-stained cells were identified by their brown:blue ratio. Data indicate increases with respect to background staining. Labels indicate non (Nil), low (Low), and high (High) microbubble exposure and radiation doses (0, 2, or 8 Gy). Treatment with 8 Gy caused a small increase above background staining. Treatments in the presence of low and high concentrations of bubbles at all radiation doses caused increases in ceramide staining. (*C*) Representative ceramide staining of sections of PC3 prostate tumors treated with radiation and/or ultrasound-activated microbubbles. Labeling is as in *A*, with the exception that sphingosine-1-phosphate (S1P, ceramide cell death inhibitor) has been added. Experiments were conducted at the higher (HMB) concentration with the addition of 0, 2, and 8 Gy of radiation. Note the lack of ceramide staining in the presence of S1P with the exposure to microbubbles and ultrasound (HMB) and 0, 2, and 8 Gy. Scale bar, 300 microns. (*D*) Quantification of ceramide immunohistochemistry staining for experiments with S1P. Data indicate an inhibition of ceramide staining in response to S1P when tumors in vivo were exposed to radiation in the presence of bubbles in comparison to data in *A*.

combined treatments could be used to decrease the total dose of radiation, which would further mitigate normal tissue radiation treatment-limiting toxicities. Lastly, these vascular disrupting ultrasound-activated microbubble treatments could be added to stereotactic high-precision radiation treatments to take advantage of vascular responses.

Materials and Methods

Mouse Tumor Experiments. Human PC3 prostate cancer (ATCC) xenografts were grown in the hind-upper leg of SCID-17 mice (Charles River) by injecting 1.0×10^6 RPMI-1640 media cultured cells subcutaneously (Wisent Biocentre), with 10% characterized serum (HyClone), and 100 U/mL of penicillin/streptomycin (Invitrogen). Tumors were grown to 7–8-mm diameter size before treatment. For treatments, ketamine and xylazine anesthetized mice were used. Vialmix device-prepared Definity microbubbles (perfluoropropane gas/liposome shell; Lantheus Medical Imaging) were administered at doses of 3.6×10^8 microbubbles (*L*, low dose) and 1.08×10^9 microbubbles (*H*, high dose) in 30-μL and 90-μL volumes of prepared bubbles, respectively. The final circulating concentrations were selected to be higher (100- and 300-fold, respectively) than the diagnostic dose used to ensure efficient interactions of the bubbles and microvascular walls.

Mice were immersed in a 37 °C water bath to permit ultrasound treatment and centered on the tumor. For ultrasound exposures, a focused central frequency 500-kHz transducer (IL0509HP; ValpeyFisher Inc.) with a 28.6-mm transducer element diameter was used. This was attached to a micropositioning system, and excited with sinusoidal wave generated by a waveform generator (AWG520; Tektronix), a pulse-receive power amplifier (RPR4000; Ritec Inc.), and a digital-acquisition system (Acquiris CC103, Agiulent Technologies NY). Tumors were exposed over 50 ms to a 16-cycle tone burst at 500-kHz and 3-kHz pulse repetition frequencies with a 10% duty cycle during the 50-ms window. Treatments were for 5 min, amounting to a 750-ms exposure over 5 min for all mouse treatments, with an average duty cycle of 0.25%. Specifically, at 500 kHz the pulse bandwidth of the 16-cycle tone burst was 0.032 ms. The pulse repetition period (3-KHz pulse repetition frequency) was 0.333 ,ms, which, over 50 ms, corresponded to 150 periods of 16-cycle tone burst or 4.8 ms (rounded to 5 ms). This 5-ms time occurred every 2 s to permit blood vessels to refill with bubbles during a treatment time of 5 min (300 s), or 150 times, for a total time of 750 ms. The ultrasound peak negative pressure was 570 kPa measured with a calibrated hydrophone. The −6 dB beamwidth was 31 mm and the −3 dB beamwidth was 18 mm.

Immediately after ultrasound exposure, mice were lead-shielded and only tumor was exposed to ionizing radiation (Faxitron Cabinet X Ray; Faxitron X Ray LLC) at doses of 0, 2, or 8 Gy in single fractions using a dose rate of 200 cGy/min.

Mice were kept for 24 h and then killed for histopathology, and a portion used for clonogenic survival assays. A second cohort of mice was used for 30-d long-term survival and growth delay analysis. A third cohort was used for micro-ultrasound power Doppler imaging. Each cohort had six mice per con-

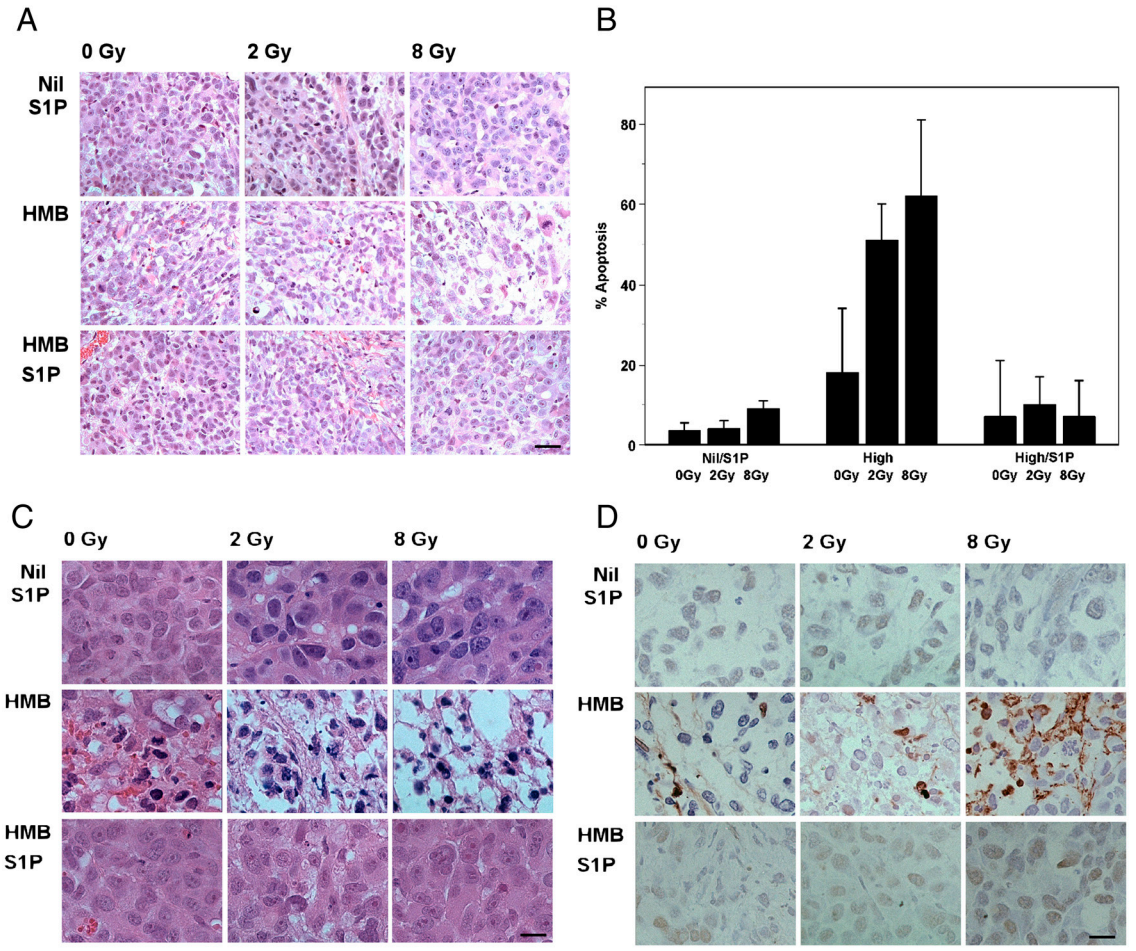

Fig. 7. In vivo histology with ceramide cell death inhibition. (*A*) Representative hematoxylin and eosin staining of sections of PC3 prostate tumors treated with radiation and/or ultrasound-activated microbubbles in the presence of sphingosince-1-phosphate. Columns represent 0, 2, and 8 Gy of radiation exposure from left to right. Rows indicate no (Nil) and high microbubble exposure (HMB), and high microbubble exposure in the presence of sphingosine-1-phosphate (S1P) from top to bottom, respectively. S1P exposure on its own had no significant effect on cell morphology. Only the 8-Gy dose showed the presence of mitotic cell death and low levels of apoptotic cell death. Bubble exposure resulted in retraction artifact and apoptosis (shown at higher magnification in *C*). Maximal disruption was evident at 8 Gy combined with bubble and ultrasound treatment. Effects were inhibited in the presence of S1P (*Bottom*). Blood vessel disruption was evident in this row but with an inhibition of death morphology. Scale bar, 90 microns. (*B*) Quantification of apoptosis. Data indicate increases in apoptotic index with treatments with respect to background levels. Labels indicate no (Nil) and high microbubble exposure (High) and radiation doses (0, 2, or 8 Gy) in the presence of sphingosine-1-phosphate (S1P). Treatment in the presence of bubbles caused the greatest increases, which were diminished in the presence of S1P. (*C*) Representative higher-magnification views of hematoxylin and eosin staining of sections of PC3 prostate tumors treated with radiation and/or ultrasound-activated microbubbles in the presence of sphingosince-1-phosphate. Panels are as organized in *A*, but at higher magnification. Focal blood vessel disruption can be seen in the HMB—0-Gy sample. Experiments conducted in the presence of S1P (*Bottom*) demonstrated a diminishment of microbubble effects with samples appearing similar to those with no treatment with ultrasound and bubbles (Nil/S1P). Scale bar, 50 microns. (*D*) Representative higher-magnification views of ISEL staining of sections of PC3 prostate tumors treated with radiation and/or ultrasound-activated microbubbles in the presence of sphingosince-1-phosphate. Note the presence of ISEL staining with bubble exposure (*Middle*) with increasing doses of radiation (as in Fig. 1). This cell death was inhibited with diminished staining in the presence of S1P (*Bottom*). Scale bar, 50 microns.

dition with 54 mice per cohort. Mice were also exposed to ultrasound alone and microbubbles alone as controls.

Timing and Exposure Experiments. For timing experiments, a delay of 0, 3, 6, 12, and 24 h was introduced between the low concentration microbubble-stimulated ultrasound treatments and the 0- and 8-Gy radiation treatment. Micro-Doppler measurements were also carried. For treatments with ultrasound-stimulated microbubbles, mice were killed at 0, 3, 6 , 12, and 24 h. For experiments in which radiation was administered, mice were killed 24 h after irradiation. For exposure experiments, 0, 0.01 low, 0.1 low, the low and high bubble concentrations, were used with no delay between the treatments. There were four mice per group.

Multiple-Fraction Experiments. For multiple-fraction experiments, mice were exposed to no treatment, ultrasound microbubble stimulation (high concentration) twice weekly on Monday and Thursday for 3 wk, and the same microbubble exposure combined with 2 Gy four times weekly, Monday to Thursday [24 Gy, BED$(10) = 28.8$ Gy]. Radiation was administered immediately after ultrasound treatments. For comparison, another group of mice received 3 Gy a day, five times weekly for 3 wk [45 Gy, BED$(10) = 58.5$ Gy] and the same 45-Gy fractionated radiation dose with ultrasound treatments given twice weekly as above. Tumor sizes were measured for up to 28 d after treatment completion, with a doubling of tumor size to 2.0-cm diameter taken as a survival endpoint in addition to standard animal care endpoints. There were $n = 5$ mice per group.

Targeted-Microbubble Experiments. For targeted experiments avidin-conjuganted MicroMarker Target-Ready Agent (VisualSonics) was used with biotinylated VEGFR2 antibody (Abcam) with a bubble concentration equivalent to that for the low-concentration Definity experiments. Unconjugated and conjugated bubbles were used for experiments with ultrasound parameters as described previously for experiments with Definity microbubbles with four PC3-bearing mice per group.

bFGF Experiments. In order to test further the importance of disrupting endothelial cells, PC3-bearing mice were treated with 0.45 μg bFGF IV (Sigma), a known endothelial cell protector, 1 h prior to exposure to microbubbles alone (1% vol/vol) in the presence of ultrasound stimulation ($n = 5$).

Ceramide and Sphingosine-1-Phosphate Experiments. In order to test if ultrasound-stimulated microbubbles in combination with ultrasound could stimulate ceramide formation, experiments were carried out using an additional cohort of 75 animals, with five mice per group. Mice were treated as above with no microbubbles, low, and high bubble concentrations in the presence of ultrasound and combined with 0-, 2-, and 8-Gy radiation doses given in single fractions as above for nine cohorts of $n = 5$ animals. In addition, 0-, 2-, and 8-Gy conditions with and without high-concentration microbubble exposure in the presence of ultrasound were carried out in the presence of S1P using modified protocols (28, 29). This used six cohorts of $n = 5$ mice.

For S1P treatments, 4 μg/g of S1P in 0.2 mL of PET (5% polyethylene glycol, 2.5% ethanol, and 0.8% Tween-80) was injected intravenously in mice 30 min prior to and 5 min after irradiation or after microbubble exposure with ultrasound and irradiation.

Histology. Samples were fixed overnight at room temperature in 1% parformaldehyde, then embedded in paraffin blocks and tumor sections cut from four equidistant regions from distal to proximal ends of the tumor. Cells were cytospinned at $2{,}000 \times g$ and fixed for 30 min. Standard hematoxylin and eosin staining and Masson's trichrome was obtained for sections and immunostaining was obtained for samples.

Micro-Ultrasound Doppler Imaging. Ultrasound imaging to detect blood in tumors before and after treatment was carried out using a VEVO-770 (Visualsonics) in power Doppler mode and a VEVO RMV transducer with a central frequency of 20 MHz. Power Doppler imaging was carried out using a step size of 0.2 mm, a wall filter of 2.5 mm/s, a scan speed of 2.5 mm/s, and a 20-dB gain setting. Doppler data were analyzed to determine vascularization index defined as the relative volume occupied by Doppler signal within a tumor volume (30) using MATLAB. Mice were anesthetized as for therapy during imaging.

Immunostaining. Immunostaining was performed using a Histostain-Plus kit (broad spectrum; Invitrogen). For ISEL and von Willebrand factor, staining was used with horseradish peroxidase-conjugated streptavidin, to bind to biotinylated secondary antibody/primary antibody and an AEC (3-amino-9-ethylcarbazole) chromagen. For more detailed staining, slides from samples were triple stained with DAPI staining for nuclear positions, CY3-conjugated CD31 for vascular delineation, and CY2-congugated TUNEL for apoptotic DNA fragmentation, and visualized with UV, 490-nm, and 550-nm light illumination, respectively. Primary antibodies were obtained from Abcam, Alexis Biochemicals, and Life Technology for anticeramide antibodies.

Light and Fluorescent Microscopy. Light microscopy of cells in solution was carried out using an inverted-stage Olympus CKX41 microscope using a 20x objective (Olympus) coupled to a U-CMAD3 video camera wired to a 2-GHz Celeron PC with an ATI external frame digitizer running ATI multimedia software (ATI-AMD). For microscopy of specimens on slides, a Leica DC100 microscope was used with a 20x objective coupled to a Leica DC100 video camera wired to a 2-GHz PC running Leica IM1000 software (Leica GmbH). For fluorescence microscopy, a Zeiss AxioImager (Zeiss) microscope was used with a 100x oil immersion objective coupled to a Microfire video camera wired to a 2-GHz PC running Stereo Investigator software (MicrobrightField Inc.).

Cell death areas were quantified in histology and immunohistochemistry tumor sections assisted by the use of Image-J (National Institutes of Health) macroscopically to detect ISEL-positive areas in tumor sections. At higher magnifications (40×), apoptotic cells were counted manually by identifying typical apoptotic bodies. For quantification of ceramide or Ki-67 immunohistochemistry, blue-to-brown ratios were used to detect presence or absence of staining through calibration to controls.

Statistical Analyses. Statistical analyses consisting of two-way ANOVA where applicable and one-way ANOVA where possible with Tukey-Kramer posttest were used in addition to nonparametric Mann–Whitney analysis where appropriate. ANOVA was used to determine effects on the basis of variance. In this analysis the observed variance in a particular variable is partitioned into components attributable to different sources of variation (other variables). This is based on a comparison of variance between items to variance within items using a sum-of-squares approach to compute variances. To indicate statistical significance, $P < 0.05$ was used (Graph Pad/InStat 3.0).

ACKNOWLEDGMENTS. G.J.C. is supported by a Cancer Care Ontario Research Chair in Experimental Therapeutics and Imaging. This research was supported by grants from the Congressionally Directed Medical Research Program, University of Toronto, and The Terry Fox Foundation. We thank Michael C. Kolios for stimulating bubble discussions.

1. Tyldesley S, et al. (2011) Estimating the need for radiotherapy for patients with prostate, breast, and lung cancers: Verification of model estimates of need with radiotherapy utilization data from British Columbia. *Int J Radiat Oncol Biol Phys* 79:1507–1515.
2. Hall EJ (2000) *Radiobiology for the Radiologist* (Lippincott Williams and Wilkins, Baltimore).
3. Paris F, et al. (2001) Endothelial apoptosis as the primary lesion initiating intestinal radiation damage in mice. *Science* 293:293–297.
4. Garcia-Barros M, et al. (2003) Tumor response to radiotherapy regulated by endothelial cell apoptosis. *Science* 300:1155–1159.
5. Rotolo J, et al. (2012) Anti-ceramide antibody prevents the radiation gastrointestinal syndrome in mice. *J Clin Invest*, 10.1172/JCI59920.
6. Sathishkumar S, et al. (2005) Elevated sphingomyelinase activity and ceramide concentration in serum of patients undergoing high dose spatially fractionated radiation treatment. *Cancer Biol Ther* 4:979–986.
7. Pena L, Fuks Z, Kolesnick R (2000) Radiation-induced apoptosis of endothelial cells in the murine central nervous system: Protection by fibroblast growth factor and sphingomyelinase deficiency. *Cancer Res* 60:321–327.
8. Moeller BJ, Cao Y, Li CY, Dewhirst MW (2004) Radiation activates HIF-1 to regulate vascular radiosensitivity in tumors. *Cancer Cell* 5:429–441.
9. Moeller BJ, et al. (2005) Pleiotropic effects of HIF-1 blockade on tumor radiosensitivity. *Cancer Cell* 8:99–110.
10. Ponce AM, Vujaskovic Z, Yuan F, Needham D, Dewhirst MW (2006) Hyperthermia mediated liposomal drug delivery. *Int J Hyperthermia* 22:205–213.
11. Moros EG, Penagaricano J, Novak P, Straube WL, Myerson RJ (2010) Present and future technology for simultaneous thermoradiotherapy of breast cancer. *Int J Hyperthermia* 26:699–709.
12. Hynynen K (2009) MRI-guided focused ultrasound treatments. *Ultrasonics* 50:221–229.
13. Jones RL, et al. (2005) Randomized trial of hyperthermia and radiation for superficial tumors. *J Clin Oncol* 23:3079–3085.
14. Tozer GM, Kanthou C, Baguley BC (2005) Disrupting blood vessels. *Nat Rev Cancer* 5:425–435.
15. Simpson DH, Burns PN, Averkiou MA (2001) Techniques for perfusion imaging with microbubble contrast agents. *IEEE Trans Ultrason Ferroelectr Freq Control* 48:1483–1494.
16. Goertz DE, Needles A, Burns PN, Foster FS (2005) High-frequency, nonlinear flow imaging of microbubble contrast agents. *IEEE Trans Ultrason Ferroelectr Freq Control* 52:495–502.
17. Goertz DE, et al. (2005) High frequency nonlinear B-scan imaging of microbubble contrast agents. *IEEE Trans Ulrason Ferroelectr Freq Control* 52:65–79.
18. Foster FS, et al. (2000) Ultrasound for the visualization and quantification of tumor microcirculation. *Cancer Metastasis Rev* 19:131–138.
19. Haag P, et al. (2006) Microbubble-enhanced ultrasound to deliver an antisense oligodeoxynucleotide targeting the human androgen receptor into prostate tumors. *J Steroid Biochem Mol Biol* 102:103–113.
20. McDannold NJ, Vykhodtseva NI, Hynynen K (2006) Microbubble contrast agent with focused ultrasound to create brain lesions at low power levels: MR imaging and histologic study in rabbits. *Radiology* 241:95–106.
21. Cosgrove D (2006) Ultrasound contrast agents: An overview. *Eur J Radiol* 60:324–330.
22. Marchesini N, Luberto C, Hannun YA (2003) Biochemical properties of mammalian neutral sphingomyelinase 2 and its role in sphingolipid metabolism. *J Biol Chem* 278:13775–13783.
23. Nikolova-Karakasjian MN, Rozenova K (2010) *Sphingolipids as Signaling and Regulatory Molecules*, eds C Chalfant and M Del Poeta (Landes Bioscience and Springer Science and Business Media, New York), pp 86–107.
24. El Kaffas A, Tran W, Czarnota GJ (2012) Vascular strategies for enhancing tumour response to radiation therapy. *Technol Cancer Res Treat* Epub ahead of print.
25. Jain RK (2005) Normalization of tumor vasculature: An emerging concept in antiangiogenic therapy. *Science* 307:58–62.
26. Caissie A, Karshafian R, Hynynen K, Czarnota GJ (2011) *Nanoimaging*, eds BA Goins and WT Phillips (Pan Standford Publishing, Boca Raton, FL), pp 267–291.
27. Krasovitski B, Frenkel V, Shoham S, Kimmel E (2011) Intramembrane cavitation as a unifying mechanism for ultrasound-induced bioeffects. *Proc Natl Acad Sci USA* 108:3258–3263.
28. Bonnaud S, et al. (2010) Sphingosine-1-phosphate activates the AKT pathway to protect small intestines from radiation-induced endothelial apoptosis. *Cancer Res* 70:9905–9915.
29. Morita Y, et al. (2000) Oocyte apoptosis is suppressed by disruption of acid sphingomyelinase gene or by sphingosine-1-phosphate therapy. *Nat Med* 6:1109–1114.
30. Huang YL, et al. (2009) Computer-aided diagnosis for breast tumors by using vascularization of 3-D power Doppler ultrasound. *Ultrasound Med Biol* 35:1607–1614.